Heterometallic spin-$\frac{1}{2}$ quantum magnet under hydrostatic pressure

M. J. Coak,[1,2] D. Kamenskyi,[3,4,5] S. P. M. Curley,[1] B. M. Huddart,[6,*] J. P. Tidey,[1] A. Chmeruk,[7,8] T. Sakurai,[9] S. Okubo,[10,†] H. Ohta,[10,†] S. Kimura,[11] H. Nojiri,[11] D. Graf,[12] S. J. Clark,[6] Z. E. Manson,[13] J. L. Manson,[13,‡] T. Lancaster,[6] and P. A. Goddard[1,§]

[1]*Department of Physics, University of Warwick, Gibbet Hill Road, Coventry CV4 7AL, United Kingdom*
[2]*School of Physics & Astronomy, University of Birmingham, Edgbaston, Birmingham B15 2TT, United Kingdom*
[3]*Department of Physics, Humboldt-Universität zu Berlin, Berlin, Germany*
[4]*Experimental Physics V, Center for Electronic Correlations and Magnetism, Institute of Physics, University of Augsburg, 86159 Augsburg, Germany*
[5]*Institute of Space Research, German Aerospace Center (DLR), 12489 Berlin, Germany*
[6]*Department of Physics, Centre for Materials Physics, Durham University, Durham DH1 3LE, United Kingdom*
[7]*Theoretische Physik III, Center for Electronic Correlations and Magnetism, Institute of Physics, University of Augsburg, 86135 Augsburg, Germany*
[8]*Augsburg Center for Innovative Technologies (ACIT), University of Augsburg, 86135 Augsburg, Germany*
[9]*Core Facility Center, The University of Osaka, Yamadaoka 2-1, Suita, Osaka 565-0871, Japan*
[10]*Molecular Photoscience Research Center, Kobe University, Hyogo 657-8501, Kobe, Japan*
[11]*Institute for Materials Research, Tohoku University, Katahira 2-1-1, Sendai, Miyagi 980-8577, Japan*
[12]*National High Magnetic Field Laboratory, Florida State University, Tallahassee, Florida 32310, USA*
[13]*Department of Chemistry and Biochemistry, Eastern Washington University, Cheney, Washington 99004, USA*

(Received 1 December 2025; revised 10 April 2026; accepted 6 May 2026; published 23 June 2026)

We investigate the properties of $CuVOF_4(H_2O)_6 \cdot H_2O$, in which two different spin species, Cu(II) and V(IV), form antiferromagnetic spin-1/2 dimers with weak interdimer coupling provided via hydrogen bonding. Using radio-frequency susceptometry and electron-spin resonance (ESR), we show how the temperature-magnetic field spin-dimer phase diagram evolves as a function of applied hydrostatic pressure and correlate this with pressure-induced changes to the crystal structure. These results, coupled with pressure-tuned DFT calculations, confirm the prior prediction that the primary exchange interaction is mediated via an unusual mechanism in which the V(IV) ions provide considerable spin density to the oxygen that joins the two spins in each dimer and which lies along the Jahn-Teller axis of the Cu(II) ion. In addition, the dissimilarity in the spins that make up each dimer unit leads to a nonlinear field dependence of the electronic energy levels as detected in the ESR measurements.

DOI: 10.1103/rlx3-z62s

I. INTRODUCTION

Symmetry breaking is an important concept throughout the natural world encompassing, among other things, issues related to the origins of matter, mass, and life [1–4]. In condensed matter physics the concept can be split into two categories: spontaneously broken symmetry, which occurs when the ground state of the system breaks a symmetry that is respected by the Hamiltonian, such as translational symmetry in crystals, rotational symmetry in ferromagnets and global phase symmetry in superconductors [5–7]; and explicitly broken symmetry in which small perturbative terms in the Hamiltonian themselves break the symmetry in question.

At low temperatures, arrays of weakly coupled Heisenberg spin-1/2 antiferromagnetic dimers adopt a quantum disordered state of spin singlets, which is separated by an energy gap from the higher lying triplet levels. A magnetic-field-induced phase transition takes place when the spins spontaneously break rotational symmetry and form a state of long-range XY magnetic order. This transition can be mapped on to the condensation of a system of bosonic or triplon excitations, whose masses can be strongly renormalized by the effect of quantum fluctuations [8–12].

$CuVOF_4(H_2O)_6 \cdot H_2O$ is a spin-1/2 dimer material, with weak interdimer coupling provided via hydrogen bonding. At ambient pressure the system displays the typical temperature-field phase diagram, hosting quantum-disordered, long-range XY-ordered and field-aligned magnetic states [13]. However, because the spin dimers are comprised of two dissimilar $S = 1/2$ ions, Cu(II) and V(IV), the magnetic Hamiltonian explic-

*Present address: Clarendon Laboratory, Department of Physics, University of Oxford, Parks Road, Oxford OX1 3PU, United Kingdom.
†Present address: Center for Life Photonic Innovation, Kobe University, Hyogo 657-8501, Kobe, Japan.
‡Deceased.
§Contact author: p.goddard@warwick.ac.uk

Published by the American Physical Society under the terms of the Creative Commons Attribution 4.0 International license. Further distribution of this work must maintain attribution to the author(s) and the published article's title, journal citation, and DOI.

itly breaks rotational symmetry in a very distinct way. Two consequences of this have previously been observed. First, the local environments around the dimerized ions do not share the same local coordinate system. This gives rise to the possibility of an anisotropic Dzyaloshinskii-Moriya (DM) interaction which can lead to the appearance of otherwise forbidden transitions ($\Delta S = \pm 1$) in electron-spin resonance (ESR) measurements [14]. Another potential cause of these transitions is the difference in g factors between the Cu and V ions that comprise the dimer unit [15]. Here, using the ESR measurements, we determine the individual g factors of the Cu(II) and V(IV) ions. Second, the primary intradimer exchange interaction is predicted to be mediated via an unusual mechanism in which the V(IV) ions provide considerable spin density to the oxygen that joins the two spins in each dimer and which lies along the Jahn-Teller axis of the Cu(II) ion [13].

Here, by performing ESR, bulk susceptometry, x-ray diffraction and density functional theory (DFT) calculations under applied pressure we show that the primary intradimer interaction strengthens with pressure up to a structural phase transition without significant change in interdimer coupling. At the structural transition, the local spin environments rotate dramatically with respect to one another, disrupting the H-bonded network that holds the dimers together, but affecting the Cu–O–V bond only marginally. The relatively small change in magnetic properties elucidated from ESR across the transition confirms that it is indeed the Cu–O–V bond that supports the primary interaction pathway and this conclusion is supported by the DFT results. The ESR spectra reveal an enhancement of the intradimer exchange interaction and modification of the g factors of Cu(II) and V(IV) ions upon applying hydrostatic pressure. Deviations from the linearity in the frequency-field dependence of the magnetic excitations allow us to disentangle the g factors of the Cu(II) and V(IV) ions.

II. METHODS

All chemical reagents for the sample synthesis were obtained from commercial sources and used as received. CuF_2 (0.4579 g, 4.51 mmol) and VF_4 (0.5724 g, 4.51 mmol) were dissolved in HF in separate plastic beakers and then combined. 2,5-methylpyrazine (0.975 g, 9.02 mmol) was added to the reaction, which was filtered twice to yield a clear green solution. Slow evaporation at room temperature yielded rectangular blue crystals around 1–4 mm on an edge. Note: hydrofluoric acid is extremely dangerous and must be handled with care, sufficient training, and appropriate personal protective equipment.

Pressure-dependent single-crystal x-ray diffraction measurements were performed at the University of Warwick using a Diacell TozerDAC turn-buckle diamond anvil cell (DAC) mounted onto a Rigaku Synergy XtaLAB Synergy-S diffractometer, equipped with a HyPix photon-counting hybrid pixel array area detector. Measurements were performed using Mo K_α radiation (0.710 73 Å) from a PhotonJet microfocus sealed tube source, allowing data to be collected to standard resolution. *In situ* pressure was determined by tracking the pressure-dependence of the fluorescence spectrum of a small ruby chip within the DAC sample chamber. Glycerol was used as the pressure transmitting medium, which has a hydrostatic limit of 5.5 GPa [16] and can hence be considered hydrostatic across the entire range of the study.

Pressure-dependent radio-frequency (RF) susceptometry measurements were performed on single crystals of $CuVOF_4(H_2O)_6 \cdot H_2O$ using a piston-cylinder cell with fields attained using a 36 T resistive magnet and 18 T superconducting magnet at the National High Magnetic Field Laboratory, Tallahasee. The pressure transmitting medium was Daphne oil 7373, which, as with the glycerol used in the x-ray measurements, provides good hydrostatic conditions in this pressure range [17]. A ruby chip located on the end of a fiber optic cable situated next to the sample provided *in situ* pressure calibration.

ESR experiments were performed using three transmission-type, multifrequency ESR spectrometers. Measurements at ambient pressure and magnetic fields up to 15 T have been performed using pulsed magnetic fields with a pulse duration of 10 msec [18]. Experiments at hydrostatic pressure up to 2.45(5) GPa and radiation frequencies up to 500 GHz were made using a 10 T superconducting magnet at Kobe University [19,20]. In both of these experiments backward wave oscillators and Gunn diodes were employed as radiation sources. A similar pressure cell was used for high-field ESR experiments up to 25 T with a cryogen-free superconducting magnet at the High Field Laboratory for Superconducting Materials (Tohoku University, Japan) [21]. In all ESR measurements, 2,2-Diphenyl-1-picrylhydrazyl (DPPH) was used as a standard magnetic field marker.

DFT calculations were performed using the approach described in Ref. [13].

III. RESULTS

A. Crystallography

The crystal structure of $CuVOF_4(H_2O)_6 \cdot H_2O$ at ambient pressure has been discussed in detail in Refs. [13,22]. Figure 1 shows the local structure around the spin-1/2 Cu(II)–V(IV) dimer units measured at 150 K at ambient pressure. At the core of the spin dimers is the vanadyl VO^{2+} ion, whose oxygen forms a covalent bond with Cu(II) along its Jahn-Teller (JT) elongated axis. Previous DFT calculations have indicated that the primary intradimer exchange interaction ($J_0 = 21.6(2)$ K, determined from susceptometry) is mediated through the vanadyl oxygen [13].

This is a highly unusual situation. It is known that Cu(II) JT bonds do not support significant exchange interactions, because the spin-density from the magnetic $d_{x^2-y^2}$ orbitals is concentrated in the plane perpendicular to this bond. In the present case, the DFT calculations suggest that the significant π bonding inherent in the vandyl ion allows for a sizable spin density to be located on the vanadyl oxygen which then supports a healthy superexchange [13]. This arrangement appears to be extremely rare among Cu and V containing compounds. In a recent study, Wang *et al.* surveyed all 522 such materials listed on the Cambridge Structural Database and found no other examples of superexchange mediated from Cu(II) to V(IV) via a single vanadyl oxygen bridge [23]. As can be seen from Fig. 1, the dimer unit also contains multiple hydro-

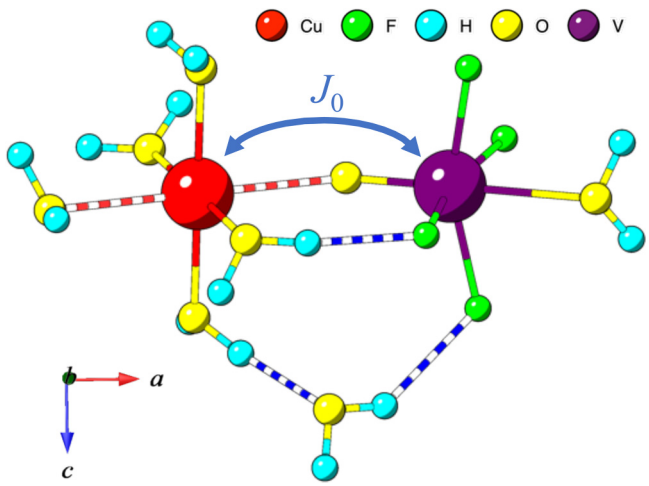

FIG. 1. Local structure of Cu(II)–V(IV) dimer units of $CuVOF_4(H_2O)_6 \cdot H_2O$ measured at 150 K using x-ray diffraction. Red striped bonds indicate the Jahn-Teller axis of the Cu(II) ion, while blue stripes highlight the intradimer hydrogen bonds. The intradimer exchange J_0 is predicted to be mediated through the central oxygen atom via an atypical exchange mechanism [13].

gen bonds. Such bonds are known to mediate superexchange in other materials [24], and so the existence of the unusual Cu–O = V exchange pathway would benefit from further experimental verification. As discussed in Ref. [13], other hydrogen bonds create Cu–O–H $\cdots$ F–V pathways [which we label as J' in Fig. 3(c)] linking the dimers together to form weakly coupled arrays in the *bc* plane. Additional H-bond pathways connect neighboring dimers within the *ab* planes.

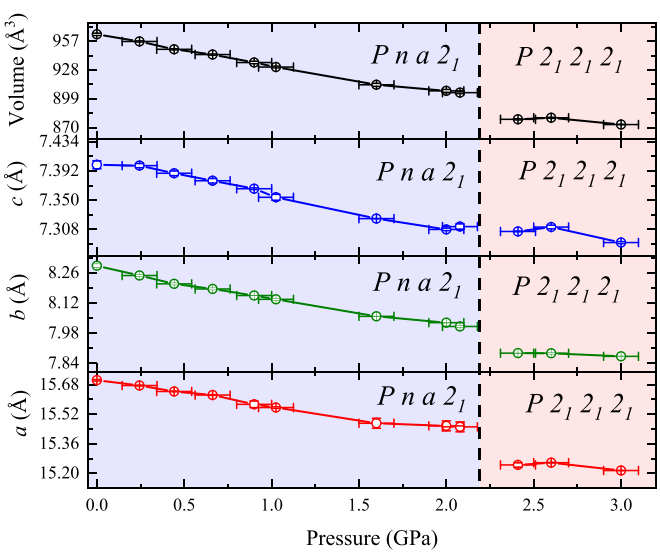

FIG. 2. Pressure dependence of the unit cell of $CuVOF_4(H_2O)_6 \cdot H_2O$ at 300 K with errors plotted at 3σ. Shaded regions highlight the low pressure $Pna2_1$ and high-pressure $P2_12_12_1$ phase, with the two regions delineated by a dashed black line. Note that in the high-pressure structural phase, the standard setting of the unit cell results in a reassignment of the *a* and *c* lattice parameters with respect to the ambient-pressure structure. In this figure, for simplicity, we have retained the ambient-pressure assignments across the phase transition.

DFT results (see Ref. [13] and later) suggest that the exchange coupling via these J'' pathways is negligible.

The crystal structure leads to the following magnetic Hamiltonian [13],

$$\mathcal{H} = J_0 \sum_i \hat{\mathbf{S}}_{1,i} \cdot \hat{\mathbf{S}}_{2,i} + \sum_{<mnij>} J'_{mnij} \hat{\mathbf{S}}_{m,i} \cdot \hat{\mathbf{S}}_{n,j} - g\mu_B \mu_0 H \sum_i \hat{S}^z_{m,i}, \quad (1)$$

where $m, n = 1,2$ label the two magnetic sites within each dimer and *i* and *j* denote neighboring dimers. The first two exchange terms represent, respectively, the intradimer exchange and the interdimer exchange through the hydrogen-bonded pathways. There is also the possibility of an additional DM interaction term in the Hamiltonian of the form $\boldsymbol{D} \cdot (\mathbf{S}_1 \times \mathbf{S}_2)$, but this is expected to be small [13]. Figure 2 shows the effect of increasing hydrostatic pressure on the unit cell of $CuVOF_4(H_2O)_6 \cdot H_2O$ up to 3.0 GPa. Below 2.1(1) GPa, the unit-cell volume compresses smoothly with no jumps or changes in slope that would suggest abrupt changes in structure. Within the pressure region $2.1 < P \leqslant 2.4$ GPa however, the system undergoes a structural phase-transition from the polar space group $Pna2_1$ to the chiral space group $P2_12_12_1$, confirmed by the systematic absences of Bragg peaks in the x-ray data at pressures $P \geqslant 2.4(1)$ GPa.

The structural effect of pressure can be investigated further by first looking at the change in the interdimer pathways. Figure 3(a) shows that, within the $Pna2_1$ phase, the interdimer Cu–O–H $\cdots$ F–V through-bond distances (filled circles) do not decrease significantly (i.e., within 3σ confidence, depicted by the error bars) upon increasing pressure, contrary to what one might expect. The true position of the electron deficient hydrogens is typically poorly defined in x-ray experiments, an issue compounded when using a pressure cell, where a significant portion of reciprocal space is obscured by the cell body. These are accordingly treated as geometrically constrained, rotating groups at standard distances, yet refine to reasonably consistent positions as seen in the geometric trends, allowing their fair assessment. To assess the effect of this issue on our conclusions, Fig. 3(a) also shows the pressure dependence of the summed direct Cu–O $\cdots$ F–V bond distances (open circles), which are seen to agree well with the Cu–O–H $\cdots$ F–V summed bond distances, indicating that, as expected, O—H bonds point almost directly at the highly electronegative F ligands.

By contrast to the through-bond interdimer exchange pathways, Fig. 3(b) shows that the through-space distances between Cu and V ions on adjacent dimer units do clearly decrease upon increasing pressure. This comes about because, as pressure brings neighboring dimer units into closer proximity, the increased repulsion between the dimers induces rotations of the water ligands. This leaves the interdimer Cu–O–H $\cdots$ F–V summed bond distances approximately constant, with only a 0.5% change across the low-pressure phase. The overall geometry of the interdimer H-bond network is also largely unchanged following the transition into the high-pressure $P2_12_12_1$ phase, see Figs. 3(c) and 3(d).

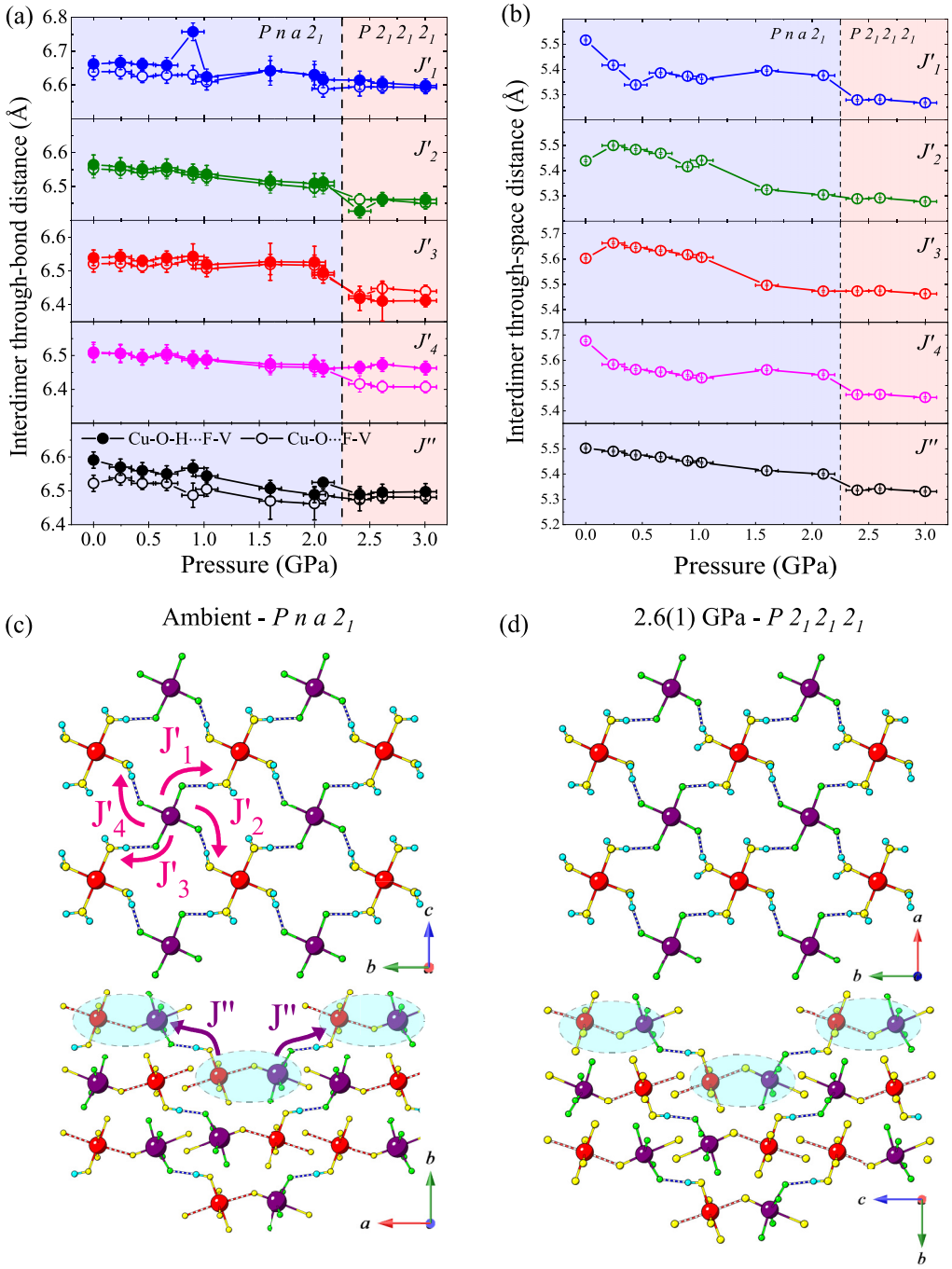

FIG. 3. (a) Pressure dependence of the interdimer exchange pathway lengths; closed circles are Cu–O–H $\cdots$ F–V and open circles are Cu–O $\cdots$ F–V bond distances, i.e., omitting the H atom (see text). (b) Pressure dependence of the through-space interdimer Cu and V distances. (c) Interdimer H-bond exchange pathway geometry in the low-pressure phase. (d) Same network for the high-pressure phase, where it can be seen to be qualitatively unchanged. Measurements are made at 300 K and errors in distances plotted at 3σ.

Figure 4(a) shows the effect increasing pressure has on the intradimer bonds. Both the Cu–O = V bond angle (top panel) and Cu–O = V through-bond distance (bottom panel) decrease gradually by around 1.5% as pressure is increased up to the structural transition. The intradimer Cu–O–H $\cdots$ F–V bond distance (middle panel) is found to be relatively unchanged up to the point of the structural phase transition; again due to rotations of the water molecules. At the transition to the high-pressure $P2_12_12_1$ phase, the intradimer Cu–O–H $\cdots$ F–V bond distance (middle panel) increases by 0.62 Å. This is due to a rotation by $\approx 45^\circ$ of the VF_4 equatorial plane relative to the CuO_4 equatorial plane about the shared axial Cu–O = V bond, as illustrated in Figs. 4(b) and 4(c). This rotation causes a significant disruption of the intradimer hydrogen bonds, but is accompanied by only a small decrease in the Cu–O = V bond angle ($\approx 5^\circ$), and the Cu–O = V through-bond distance ($\approx 0.03(2)$ Å).

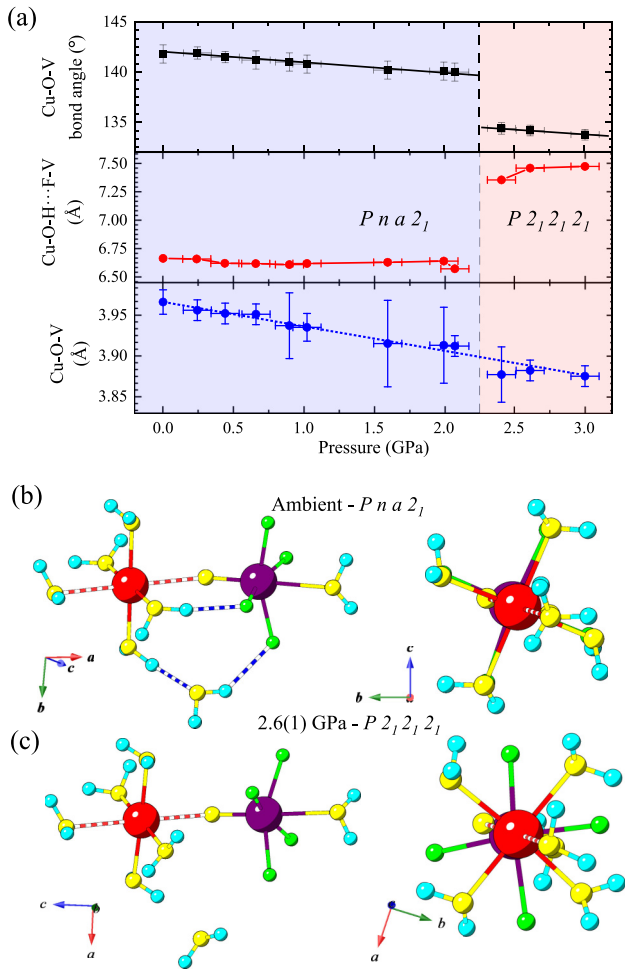

FIG. 4. (a) Pressure dependence of the intradimer Cu—O—V summed bond distance (bottom panel), intradimer Cu–O–H $\cdots$ F–V bond distance (middle panel) and Cu—O—V bond angle (top panel). Structure of the dimer unit in the low-pressure (b) and high-pressure (c) phase. The views along the dimer axis on the right show that a key difference between the structures is a rotation by $\approx 45^\circ$ of the VF_4 plane relative to the CuO_4. Measurements made at 300 K and errors on the vertical axes plotted at 3σ.

B. Density functional theory

To help understand the differences in the strength of the magnetic exchange following the application of pressure, we used DFT to calculate the spin density distribution for the $p = 2.6$ GPa structure. The DFT parameters used for these calculations are the same as those used for the ambient pressure structure, which can be found in the Supplemental Material of Ref. [13]. Figure 5 shows the spin-density distribution calculated for two different magnetic structures for both the ambient and 2.6 GPa crystal structures, i.e., above and below the experimentally observed structural phase transition. In the magnetic structure labeled AFM1, all of the nearest-neighbor Cu–V couplings are antiferromagnetic, whereas in AFM3 the intradimer coupling is ferromagnetic, while all couplings between dimers are kept antiferromagnetic. These two magnetic states can be used in combination to calculate the magnitude of the intradimer exchange.

The antiferromagnetic state AFM1 is found to remain the magnetic ground state of the system at 2.6 GPa. The spin-density distributions are very similar to those for the ambient pressure structure, with the most significant difference being changes in the direction in which the lobes of the spin density on the Cu and V ions point. The spin-density isosurfaces in the vicinity of Cu and V reflect the shapes of the magnetically active orbitals on these ions, whose directions move with the rotation of the equatorial ligands that accompanies the structural phase transition. Mulliken analysis reveals some changes in the total spin on the atoms after applying pressure. The moments on the Cu and V ions decrease to 0.62 and 1.21 μ_B, respectively, from their values 0.65 and 1.29 μ_B for the ambient-pressure structure. Details of the moment sizes for each magnetic structure considered are given in the Appendix. The spin density on the O atoms joining Cu and V within a dimer, which we previously suggested to play a significant role in mediating the intradimer exchange, also decreases, from 0.26 to 0.21 μ_B. Despite this, the relative energies of the magnetic states AFM1 and AFM3 leads to an estimate of $J_0 = 29.6$ K for the intradimer exchange, a slight increase over the value $J_0 = 24.7(6)$ K calculated for the ambient-pressure structure. While this is in qualitative agreement with experiment (see below), we also find that the calculated interdimer exchange J'_{1-4} increases significantly, from 8.6 to 33.0 K, which is not reproduced in experiment. We note that, even at ambient pressure, DFT was found to significantly overestimate J'_{1-4} which was found to be ≈ 1 K in experiment, with the DFT value also being very strongly dependent on the Hubbard U used in the calculations [13]. This, coupled with the huge increase in J'_{1-4} calculated for the high-pressure phase, suggests that the interdimer exchange J'_{1-4} is poorly described by DFT. The other interdimer exchange J'' remains sufficiently small that it cannot be determined accurately.

We note that these results were obtained using a Hubbard U of 5 eV on the Cu and V d orbitals, the value which was found to give the best agreement with experiment for the intradimer exchange J_0 in the ambient-pressure structure [13]. However, it is possible that a different value of U could result in better agreement with experiment for the 2.6 GPa structure. Investigating the effect of Hubbard U on the calculated exchange constants for the 2.6 GPa structure, along with systematic investigations of the effect of pressure on the exchange constants obtained using DFT, are likely to be instructive but are beyond the scope of this study.

C. High-pressure susceptometry

The top panel of Fig. 6(a) shows the field dependence up to 23 T of the differential susceptibility dM/dH for a single crystal of $CuVOF_4(H_2O)_6 \cdot H_2O$ at the lowest temperature measured for each pressure, at ambient pressure, 1.5(1) and 2.0(1) GPa, using the RF susceptometry technique [25–27]. The magnetic field was oriented close to parallel with the a axis of the crystal. Typically in $S = 1/2$ dimer systems, sharp cusps are observed in dM/dH at the critical fields H_{c1} and H_{c2} [28,29] that respectively mark the transition from

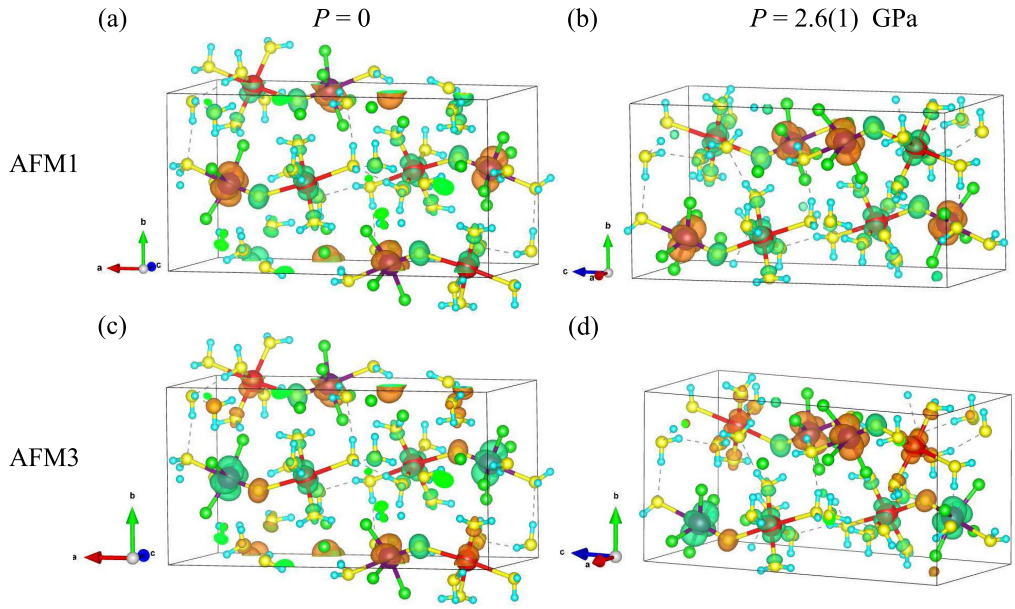

FIG. 5. Spin-density distribution obtained from DFT for the two magnetic states that determine the strength of the intradimer exchange J_0. Orange and green isosurfaces represent regions with significant positive and negative spin density, respectively. These are shown for the ambient pressure structure in (a) and (c), and for the $p = 2.6(1)$ GPa structure, in (b) and (d).

quantum disorder to field-induced magnetic order and then to the field-polarized phase. In the present case, the data instead exhibit two broad peaklike features similar to those observed in Ref. [13]. It was suggested there that the broad nature of the features in $\mathrm{d}M/\mathrm{d}H$ observed at ambient pressure in this material could arise due to H-bond disorder within the complex interdimer exchange network, giving rise to a distribution in the superexchange between neighboring dimers and a smearing of the transition features in $\mathrm{d}M/\mathrm{d}H$.

The profile of the $\mathrm{d}M/\mathrm{d}H$ curves is qualitatively similar at low and high pressures, but the peaklike features are both shifted to higher fields as pressure increases. The bottom panel shows the trough and peak features seen in the second differential of the magnetization, which can be used to determine the positions of H_{c1} and H_{c2}, respectively [13]. At 2.0(1) GPa, $H_{c1} = 16.4(2)$ T and $H_{c2} = 21.5(2)$ T, an increase of ≈ 3 T in both values compared to the ambient data. The difference between the two critical fields ($\Delta H = H_{c2} - H_{c1}$) at 2.0(1) GPa and 0.34 T is $\Delta H = 5.1(3)$ T, which is the same to within error as the ambient pressure value of $\Delta H = 5.5(3)$ T; this is true for all five pressures at which susceptometry measurements were performed between ambient and 2.0(1) GPa. At each pressure, $\mathrm{d}M/\mathrm{d}H$ was measured as a function of field at different temperatures for all pressures. The two peaklike features are seen to move closer with increasing temperatures, becoming unresolvable as separate features around 2 K for all measured pressures.

Also shown in Fig. 6(a) are the susceptometry data taken at 2.4(1) GPa, which is higher than the critical pressure for the structural transition. Experimental constraints limit the field for this measurement to less than 18 T. This means that while the onset to the lower-field transition at H_{c1} is observed, the transition at H_{c2} is beyond the accessible field range. Nevertheless, it is seen that the slow increase in H_{c1} with pressure observed at lower pressures seems to be continued at 2.4(1) GPa. Certainly, the structural transition does not lead to a sudden drop in H_{c1} as might be expected if the intradimer exchange was mediated by the hydrogen-bond network, which is significantly disrupted at the structural transition.

The temperature dependence of the extracted H_{c1} and H_{c2} values allows the pressure-evolution of the temperature-field phase-diagram to be tracked, with the results shown in Fig. 6(b). A dome of field-induced XY magnetic order is observed at all pressures, lying between the low-field quantum disordered and high-field field-polarized phases. The midpoint of the dome increases steadily with increasing pressure, but its width remains largely unchanged up to 2.0(1) GPa. This implies that the intradimer exchange strengthens under pressure, while the interdimer coupling stays roughly constant. Measurements of the pressure evolution of the g factors are required to extract quantitative values for exchange energies. This process is discussed below.

D. High-pressure electron spin resonance

Here, we expand the previous ESR study of $CuVOF_4(H_2O)_6 \cdot H_2O$ [13] to encompass magnetic fields above H_{c2} and perform measurements at hydrostatic pressures up to 2.45(5) GPa. Figure 7(a) shows the ambient pressure ESR spectra taken in a 25 T superconducting magnet at 50 and 135 GHz when the magnetic field is applied along the dimer axis ($H \parallel a$). We can identify five absorption peaks: τ, G_1, G_2, M, and U which originate from the Cu-V dimer system.

As shown previously by temperature dependent ESR measurements [13], the τ mode corresponds to transitions ($\Delta S_z = \pm 1$) that occur within the excited $S = 1$ triplet state [see energy level diagram in inset of Fig. 7(b)]. There are a few small peaks in the vicinity of τ, which we attribute to low levels of Cu^{2+} and V^{4+} impurities [13].

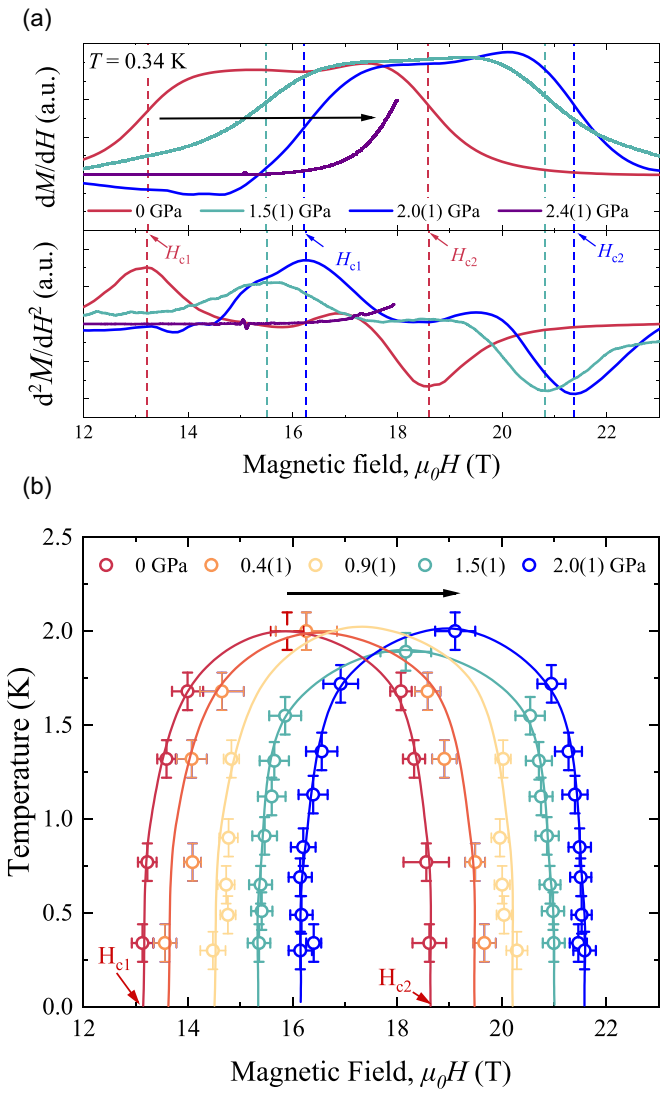

FIG. 6. (a) Field-dependent differential susceptibility dM/dH measured using radio-frequency susceptometry at the lowest temperature measured, at ambient pressure, 1.5(1), 2.0(1), and 2.40(10) GPa. The arrow illustrates the shift of features to higher field as pressure is increased. Critical fields at each pressure are determined from the positions of peaks and troughs in differentiated data (d^2M/dH^2) and indicated with dashed lines. (b) Positions of the critical fields map out the pressure dependence of the temperature-field phase diagram of $CuVOF_4(H_2O)_6 \cdot H_2O$.

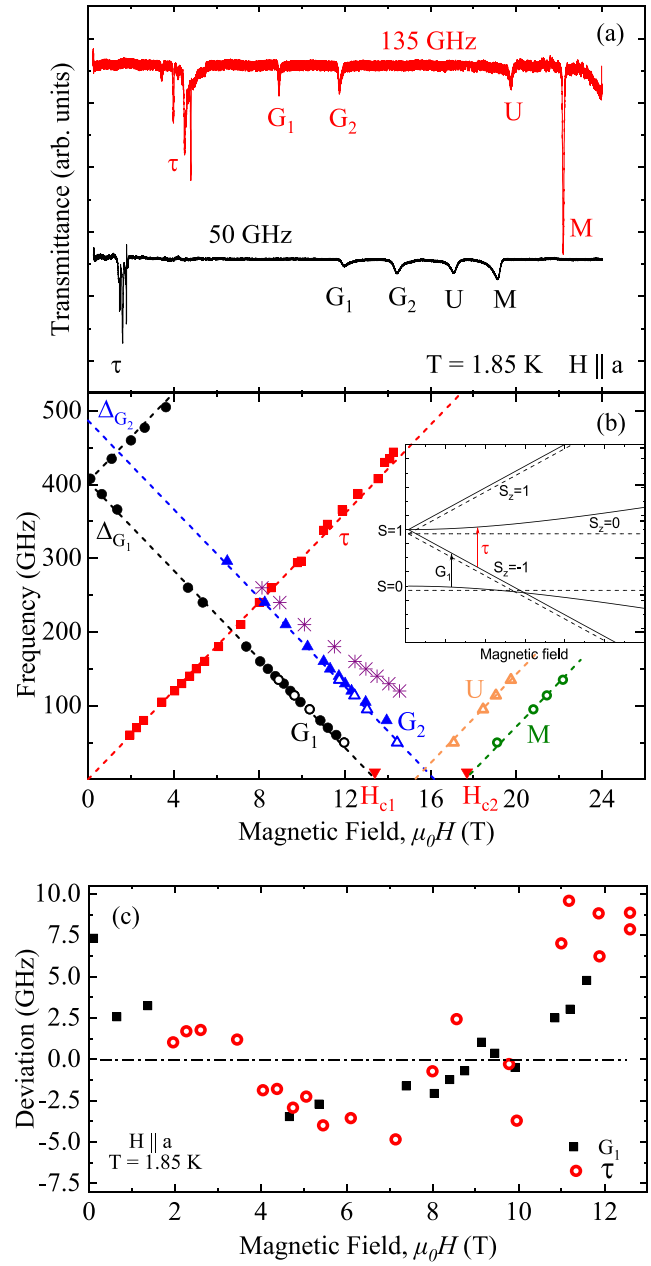

FIG. 7. Ambient pressure ESR data. (a) ESR spectra of $CuVOF_4(H_2O)_6$ measured at different radiation frequencies at 1.85 K and $H \parallel a$. (b) Frequency-field dependence of the ESR transitions measured at 1.85 K and $H \parallel a$. Red triangles show critical fields determined from d^2M/dH^2 data [Fig. 6(b)]. Closed symbols are the data from Ref. [13], while open symbols show the extended dataset obtained at the 25 T facility at Tohoku University. All observed resonances, including those marked with purple stars, are described in the text. The inset compares the energy levels of a dimer system composed of two ions with the same g factor (dashed lines) with that of ions with different g values (solid lines). Arrows indicate the modes G_1 and τ observed in the experiments. (c) Difference between the experimental data for modes G_1 (black) and τ (red) and their linear fits, with $\Delta G_1 = 404$ GHz and $g_{\text{eff}} = 2.15$.

The frequency variation of the peak positions, the so-called frequency-field diagram (FFD), is shown in Fig. 7(b). The energy of the G_1 mode decreases with magnetic field and reaches zero close to H_{c1} determined from the RF susceptometry, indicating that it arises from transitions between the singlet ground state $S = 0$ and the $S_z = -1$ state. ESR measurements are sensitive to transitions at the Γ point ($k = 0$) because the radiation used carries a negligible momentum k. Hence, the critical field at which the singlet-triplet energy gap closes extracted from ESR can be higher than that from bulk magnetometry, which is sensitive to the whole Brillouin zone.

The slope of the dashed lines in Fig. 7(b) yields the effective g factor of 2.15(1), which is the average value of the g factors of the Cu^{2+} and V^{4+} ions that form the dimers. There is a clear departure from linear-in-field behavior of the G_1 and τ modes [see Fig. 7(c)]. This is a characteristic feature

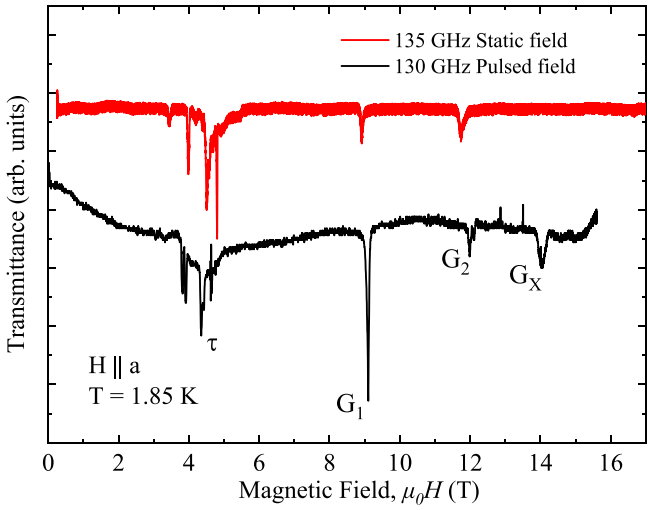

FIG. 8. Ambient pressure, 1.85 K ESR spectra of $CuVOF_4(H_2O)_6$ measured in pulsed (black line) and quasistatic magnetic fields (red line) at 130 and 135 GHz, respectively, for $H \parallel a$.

of a spin-dimer system formed by dissimilar spins. While the overall slope corresponds to the average g factor of Cu^{2+} and V^{4+}, the nonlinearity is dictated by the difference between them [15].

The inset in Fig. 7(b) illustrates the difference between the energy level schemes for dimer systems with similar (dashed lines) and dissimilar (solid lines) magnetic ions. The field behavior of the $S_z = 0$ and $S = 0$ states is distinctly nonlinear for the system of dissimilar spins; thus, the experimentally observed deviation from linearity allows us to disentangle the Cu^{2+} and V^{4+} g factors. A least squares fit returns $g_V = 2.00(5)$ and $g_{Cu} = 2.30(5)$. We note that the presence of a DM interaction may also lead to the nonlinear behavior of the G_1 mode, depending on the relative orientation of the DM vector. However, the deviation from the linearity in the case of a DM interaction is much more pronounced in the vicinity of the H_{c1}, while here we observe it over the entire field range [30].

The M mode appears close to H_{c2} and grows linearly with increasing field. It is attributed to the excitation of magnons emerging from the field-polarized phase. Following the same Brillouin zone argument above, the field at which this mode reaches zero frequency can be lower than the upper critical field obtained from bulk measurements.

The triplet excitations in a system of equivalent dimers appear in the ESR spectrum as a single gapped mode. Additional G_n modes in the spectra with the same slope as G_1 have therefore previously been ascribed to the presence of more than one nonequivalent dimer systems in the unit cell, leading to the formation of additional triplet branches [14,31–35]. Following this example, we attribute the G_2 mode to the excitations of a second triplet branch. Transitions indicated by purple stars in Fig. 7(b) are only observed in the pulsed-field ESR experiments and are absent in quasistatic field measurements (see resonance G_X in Fig. 8). This mode has a pronounced nonlinear magnetic field behavior and appears in the vicinity of H_{c1}. Although the exact origin of these excitations is unclear at the moment, we suspect that it may appear due to magnetostrictive and magnetocaloric effects, which typically become quite strong close to the critical field. These effects have been observed before in studies of dimer systems, particularly in the high dH/dt provided by pulsed magnets [29,36].

The intensity of the U mode observed at fields between G_2 and M decays as the frequency grows and the resonance shifts beyond H_{c2} [shown with orange symbols in Fig. 7(b)]. The excitation spectrum in the XY-ordered phase is formed by the excited triplons and the intricate network of interactions between them and is known to support multiple ESR resonances. For example, very complicated ESR spectra between H_{c1} and H_{c2} have been reported in $Ba_3Cr_3O_8$ [35] and $SrCu_2(BO_3)_2$ [30,37].

Figure 9 illustrates the changes in the ESR spectra caused by hydrostatic pressure for $H \parallel a$, measured at frequencies both above and below the zero-field singlet-triplet gap, $\Delta_{G_1} \approx 400$ GHz at ambient pressure. For frequencies above the gap (panel (a), $\nu = 497$ GHz), the G_1 mode shifts towards lower magnetic fields with increasing pressure, while below the gap (panel (b), $\nu = 180$ GHz) it shifts to higher fields, which suggests that Δ_{G_1} increases with pressure. Panel (c) compares high-field ESR spectra at ambient and above critical pressure. The spectra remain qualitatively unchanged by the structural transformation but the resonances are shifted to higher field values at the higher pressure.

The pressure also affects the g factor through modifications to the local spin environment. The constraints of the pressure experiments means that is not possible to disentangle the Cu^{2+} and V^{4+} g factors individually at elevated pressures with acceptable accuracy, but the effective g factor for the dimer unit can be ascertained. The parameters extracted from the ESR data are discussed in detail below in comparison to the susceptometry results.

IV. DISCUSSION

Figure 10 displays the effect of hydrostatic pressure on the magnetic parameters of $CuVOF_4(H_2O)_6 \cdot H_2O$ for magnetic fields applied along a. The vertical dashed line in the figure indicates the critical pressure of the structural phase transition described above. Panel (a) shows the effective dimer g factor extracted from ESR. A gradual monotonic decrease is observed on increasing pressure from 2.15(1) at ambient pressure to 1.90(3) at 2.0(2) GPa. At the structural transition, the local spin environment undergoes a significant reconfiguration and the g factor measured at 2.45(5) GPa increases sharply to 2.14(3), the same as the ambient pressure value within experimental uncertainty. The zero-field singlet-triplet gap, Δ_{G1}, increases linearly with pressure, see panel (b). However, unlike the g factor, this parameter shows only a small deviation from this linear behavior on passing through the structural transition.

Figure 10(c) shows the pressure dependence of the critical fields $\mu_0 H_{c1}$ and $\mu_0 H_{c2}$ extracted from RF susceptometry measurements by extrapolating the finite-temperature critical-field values to zero temperature (solid symbols). Respectively, these are the end of the quantum-disordered phase and the onset of the field-saturated phase and hence demark the zero-temperature bounds of the dome of field-induced XY-order

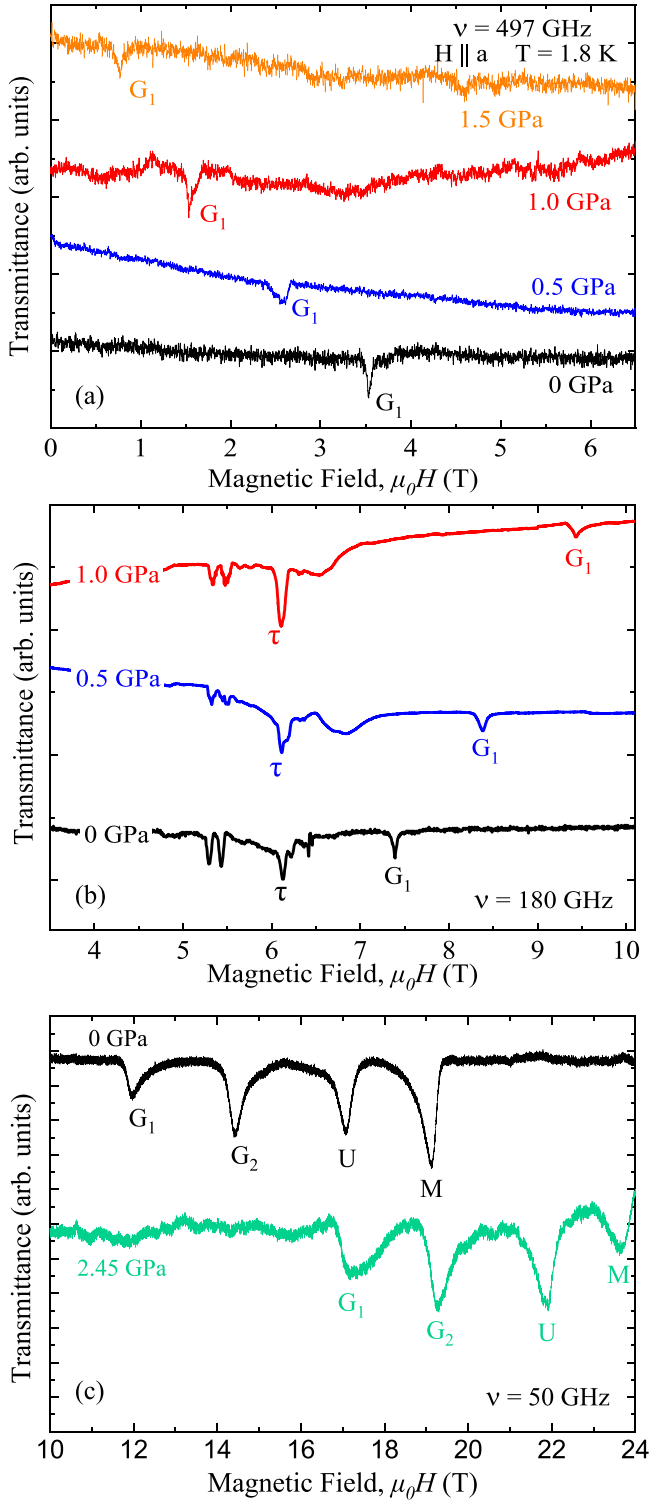

FIG. 9. Example 497 GHz (a), 180 GHz (b), and 50 GHz (c) ESR spectra of $CuVOF_4(H_2O)_6$ measured at different hydrostatic pressures, $T = 1.8$ K and $H \parallel a$. The spectra at 50 GHz and 2.45(5) GPa [shown in green on panel (c)] are measured above the critical pressure for the structural transformation.

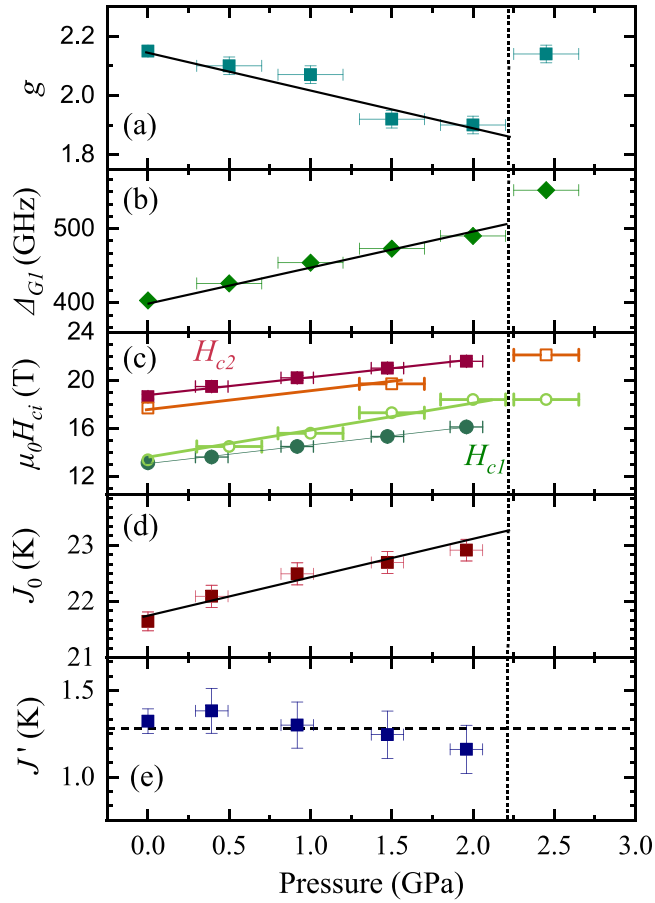

FIG. 10. Pressure dependence of the magnetic parameters. (a) Effective g factor extracted from ESR. (b) Triplet-singlet energy gap, Δ_{G1}, extracted from ESR. (c) Values of critical fields H_{c1} and H_{c2}, found from extrapolating the susceptometry-derived data in Fig. 6 to zero temperature (solid symbols) and from the zero-frequency intercepts of the G_1 and M ESR modes (open symbols). (d) Values of intradimer exchange J_0 and (e) effective interdimer exchange J' calculated from Eq. (2). The vertical dashed line indicates the pressure-induced structural phase transition.

shown in Fig. 6. As can be seen, both critical fields increase linearly with pressure at roughly the same rate, indicating that, as mentioned earlier, the dome moves higher in field with applied pressure, but does not change in width. Also shown in panel (c) are the critical fields as deduced from ESR measurements (open symbols). In this case, the lower and upper critical fields are defined as the field at which the G_1 and M ESR modes reach zero frequency, respectively. The M mode was only observed in a subset of the pressure measurements, those where high fields were employed. Given the fact, discussed above, that ESR is sensitive only to $k = 0$ transitions, these fields need not be identical to, but should lie within those extracted from susceptometry. This is what we observe and, in fact, there is a reasonably close agreement between the critical fields determined from the two techniques.

Within the model of weakly interacting dimers, the critical fields are determined by the exchange energies via the relations [38]

$$g\mu_B\mu_0 H_{c1} = J_0 - nJ'/2, \quad g\mu_B\mu_0 H_{c2} = J_0 + nJ'. \qquad (2)$$

Here J_0 is the primary, intradimer exchange defined in Eq. (1), J' is the effective interdimer interaction strength (the average of J'_{1-4}) and $n = 4$ is the number of interdimer neighbors as

described above. This is the same model previously used to describe the ambient pressure properties of $CuVOF_4(H_2O)_6 \cdot H_2O$ [13]. Using the critical fields extracted from RF susceptometry and the g factors from ESR, the pressure dependence of the exchange energies can be determined and are shown in Figs. 10(d) and 10(e). At ambient pressure, both interaction strengths are found to be the same as reported in Ref. [13].

Up to 2.0(1) GPa, pressure has little effect on the magnitude of the interdimer exchange J', which remains constant within experimental uncertainty at $J' \approx 1.3(1)$ K. This is in line with high-pressure structural measurements, which show that while pressure does bring the dimer units into closer proximity, the overall geometry and length of the interdimer exchange pathways is nearly unchanged up to 3.0 GPa; see Fig. 3. In contrast, the magnitude of J_0 is seen to increase linearly with pressure, reaching a maximum measured value of 22.9(2) K at 2.0(1) GPa within the low-pressure structural phase. This increase is due to decreases in both the Cu—O—V bond length and angle [see Fig. 4(a)] and is in agreement with the trend found by the DFT calculations.

It is not possible to follow the trends in J_0 and J' through the pressure-induced structural phase transition because H_{c2} grows larger than the available magnetic field. However, the singlet-triplet gap determined from ESR [Fig. 10(b)] shows only a small deviation at the structural transition from the slow increase seen within the low-pressure phase, indicating that there is no radical change in the size of J_0 at the structural phase transition. This observation provides additional strong evidence for the role of intradimer oxygen in the exchange pathway. As discussed above, the summed intradimer Cu—O—V bond distance decreases only slightly across the transition, and the bond-angle reduces by $\approx 5^\circ$ when moving from 0 to 2.0(1) GPa [Fig. 4(a)]. On the other hand, the structural phase-transition induces a rotation of the equatorial ligands on each ion about the Cu–O–V bond, see Figs. 4(b) and 4(c). This is reflected in the significant change in the g factor at the transition [Fig. 10(a)]. The rotation causes a drastic increase in the length of the summed intradimer Cu–O–H $\cdots$ F–V bond pathway by 0.62(2) Å at the onset of the phase transition. If this were the primary exchange pathway, then a significant change would be expected in the intradimer exchange and hence also the singlet-triplet gap, which is not observed. Instead, the strong J_0 must be accounted for via the highly unusual mechanism suggested in Ref. [13] in which the intradimer superexchange is mediated along the Cu(II) JT axis to V(IV) via a single vanadyl oxygen bridge.

In summary, we find that the primary exchange energy in the quantum magnet $CuVOF_4(H_2O)_6 \cdot H_2O$ is enhanced by applied hydrostatic pressure up to and across a structural phase transition at around 2.4 GPa, while the interdimer exchange changes only slightly. This is consistent with the pressure-induced modifications observed in the bond distances and the g factors. The effect of the dissimilarity of the spins in the dimer unit is seen in the ESR transition energies, which exhibit a nonlinear field dependence, as well as several unidentified resonances. It remains to be seen if other spin-1/2 copper-vanadium compounds can be identified that host exchange interactions mediated through the oxygen atom on the distorted JT axes.

ACKNOWLEDGMENTS

We thank J. Villa for useful discussions, as well as T. Orton and P. Ruddy for technical assistance. This project has received funding from the European Research Council (ERC) under the European Union's Horizon 2020 research and innovation programme (Grant Agreement No. 681260). A portion of this work was performed at the National High Magnetic Field Laboratory (NHMFL), which is supported by National Science Foundation Cooperative Agreements No. DMR-1644779 and No. DMR-2128556 and the Department of Energy (DOE). M.J.C. is supported by a UKRI Future Leaders Fellowship, Grant No. MR/Y016602/1. T.L. is supported by EPSRC (UK) through Grant No. EP/Z534067/1. This work has made use of the Hamilton HPC Service of Durham University. Work at Durham was supported by the EPSRC UK Skyrmion Project under Grant No. EP/N032128/1 B.M.H. is supported by UK Research and Innovation (UKRI) under the UK Government's Horizon Europe funding guarantee (Grant No. EP/X025861/1). The work at EWU was supported by the NSF through Grant No. DMR-2104167. High-field ESR experiments were performed at the High Field Laboratory for Superconducting Materials, Institute for Materials Research, Tohoku University (GIMRT No. 20K0603 and No. 20H0507). Part of the high-pressure ESR experiments was conducted at the Molecular Photoscience Research Center, Kobe University. Support of the ICC-IMR Visitor Program at Tohoku University is acknowledged. T.S. acknowledges the support provided by the JSPS KAKENHI Grant No. 23K03321. D.K. was supported by the PRIME program of the German Academic Exchange Service (DAAD) with funds from the German Federal Ministry of Education and Research (BMBF). D.K. and A.C. thank the Deutsche Forschungsgemeinschaft (DFG, German Research Foundation)–TRR 360 (Project No. 492547816) for supporting this work.

DATA AVAILABILITY

Data presented in this paper are available at [39].

TABLE I. DFT calculations details – Local magnetic moments (in Bohr magnetons) on Cu and V for the FM and AFM configurations. Moments are listed separately for ions with positive spin density and those with negative spin density.

	Cu		V	
Configuration	+	−	+	−
FM	0.622	0.622	1.198	1.198
AFM1	0.624	0.624	1.205	1.205
AFM2	0.626	0.625	1.208	1.207
AFM3	0.610	0.617	1.196	1.197
AFM4	0.618	0.617	1.199	1.199
AFM5	0.619	0.618	1.206	1.206

APPENDIX: DFT CALCULATIONS – ADDITIONAL DETAILS ON MAGNETIC MOMENTS OF EACH SPIN CONFIGURATION

For the DFT results presented in the main text, the moments on each of the ions in each spin configuration were calculated using Mulliken population analysis, and the results are shown in Table I. We see that the variation in the moment size across configurations is small, with the total variation in the Cu moment (range divided by mean) being around 3%, while the V moments are even more consistent, with these agreeing to within 1%. For some antiferromagnetic (AFM) configurations, we calculated a slightly different moment for those ions having a net positive spin density compared to those having a negative spin density, which might suggest that some of these AFM configurations have net magnetization. However, in these cases, the total moment of the unit cell is $<2 \times 10^{-5}$ μ_B, indicating that the spin density on the other atoms in the system compensates for this imbalance.

[1] D. C. Krakauer, Symmetry–simplicity, broken symmetry–complexity, Interface Focus **13**, 20220075 (2023).

[2] L. Canetti, M. Drewes, and M. Shaposhnikov, Matter and antimatter in the universe, New J. Phys. **14**, 095012 (2012).

[3] P. W. Higgs, Broken symmetries and the masses of gauge bosons, Phys. Rev. Lett. **13**, 508 (1964).

[4] P. Sandars, Chirality in the RNA world and beyond, Int. J. Astrobiol. **4**, 49 (2005).

[5] P. W. Anderson, *Basic Notions of Condensed Matter Physics*, 2nd ed. (Westview Press, 1997).

[6] L. D. Landau, On the theory of phase transitions, Zh. Eksp. Teor. Fiz. **7**, 19 (1937).

[7] S. Weinberg, Superconductivity for particular theorists, Prog. Theor. Phys. Suppl. **86**, 43 (1986).

[8] V. Zapf, M. Jaime, and C. D. Batista, Bose-Einstein condensation in quantum magnets, Rev. Mod. Phys. **86**, 563 (2014).

[9] A. Oosawa, M. Ishii, and H. Tanaka, Field-induced three-dimensional magnetic ordering in the spin-gap system, J. Phys.: Condens. Matter **11**, 265 (1999).

[10] C. Rüegg, N. Cavadini, A. Furrer, H.-U. Güdel, K. Krämer, H. Mutka, A. Wildes, K. Habicht, and P. Vorderwisch, Bose–Einstein condensation of the triplet states in the magnetic insulator $TlCuCl_3$, Nature (London) **423**, 62 (2003).

[11] M. Jaime, V. F. Correa, N. Harrison, C. D. Batista, N. Kawashima, Y. Kazuma, G. A. Jorge, R. Stern, I. Heinmaa, S. A. Zvyagin, Y. Sasago, and K. Uchinokura, Magnetic-field-induced condensation of triplons in Han Purple pigment $BaCuSi_2O_6$, Phys. Rev. Lett. **93**, 087203 (2004).

[12] M. J. Coak, S. P. M. Curley, Z. Hawkhead, J. P. Tidey, D. Graf, S. J. Clark, P. Sengupta, Z. E. Manson, T. Lancaster, P. A. Goddard, and J. L. Manson, Asymmetric phase diagram and dimensional crossover in a system of spin-$\frac{1}{2}$ dimers under applied hydrostatic pressure, Phys. Rev. B **108**, 224431 (2023).

[13] S. P. M. Curley, B. M. Huddart, D. Kamenskyi, M. J. Coak, R. C. Williams, S. Ghannadzadeh, A. Schneider, S. Okubo, T. Sakurai, H. Ohta, J. P. Tidey, D. Graf, S. J. Clark, S. J. Blundell, F. L. Pratt, M. T. F. Telling, T. Lancaster, J. L. Manson, and P. A. Goddard, Anomalous magnetic exchange in a dimerized quantum magnet composed of unlike spin species, Phys. Rev. B **104**, 214435 (2021).

[14] M. Matsumoto, T. Shoji, and M. Koga, Theory of magnetic excitations and electron spin resonance for anisotropic spin dimer systems, J. Phys. Soc. Jpn. **77**, 074712 (2008).

[15] A. Abragam and B. Bleaney, *Electron Paramagnetic Resonance of Transition Ions* (Clarendon press, Oxford 1970), p. 509.

[16] S. Klotz, K. Takemura, T. Strässle, and T. Hansen, Freezing of glycerol–water mixtures under pressure, J. Phys.: Condens. Matter **24**, 325103 (2012).

[17] S. Klotz, J.-C. Chervin, P. Munsch, and G. Le Marchand, Hydrostatic limits of 11 pressure transmitting media, J. Phys. D **42**, 075413 (2009).

[18] H. Ohta, M. Tomoo, S. Okubo, T. Sakurai, M. Fujisawa, T. Tomita, M. Kimata, T. Yamamoto, M. Kawauchi, and K. Kindo, Recent developments of high field ESR systems in Kobe, J. Phys.: Conf. Ser. **51**, 611 (2006).

[19] T. Sakurai, A. Taketani, T. Tomita, S. Okubo, H. Ohta, and Y. Uwatoko, Development of high-pressure, high-field and multifrequency electron spin resonance system, Rev. Sci. Instrum. **78**, 065107 (2007).

[20] R. Okuto, E. Ohki, T. Sakurai, K. Hijii, H. Takahashi, E. Ohmichi, S. Okubo, H. Ohta, Y. Uwatoko, and H. Tanaka, Development of high-field and high-pressure ESR system and application to triangular antiferromagnet $CsCuCl_3$, Appl. Magn. Res. **50**, 1059 (2019).

[21] T. Sakurai, S. Kimura, M. Kimata, H. Nojiri, S. Awaji, S. Okubo, H. Ohta, Y. Uwatoko, K. Kudo, and Y. Koike, Development and application of 2.5 GPa – 25 T high-pressure high-field electron spin resonance system using a cryogen-free superconducting magnet, J. Magn. Reson. **296**, 1 (2018).

[22] M. D. Donakowski, R. Gautier, J. Yeon, D. T. Moore, J. C. Nino, P. S. Halasyamani, and K. R. Poeppelmeier, The role of polar, lamdba-shaped building units in noncentrosymmetric inorganic structures, J. Am. Chem. Soc. **134**, 7679 (2012).

[23] Y. Wang, M. Fukuda, S. Nikolaev, A. Miyake, K. J. Griffith, M. L. Nisbet, E. Hiralal, R. Gautier, B. L. Fisher, M. Tokunaga, M. Azuma, and K. R. Poeppelmeier, Two distinct Cu(II)–V(IV) superexchange interactions with similar bond angles in a triangular CuV_2 fragment, Inorg. Chem. **61**, 10234 (2022).

[24] P. A. Goddard, J. Singleton, C. Maitland, S. J. Blundell, T. Lancaster, P. J. Baker, R. D. McDonald, S. Cox, P. Sengupta, J. L. Manson, K. A. Funk, and J. A. Schlueter, Isotope effect in quasi-two-dimensional metal-organic antiferromagnets, Phys. Rev. B **78**, 052408 (2008).

[25] G. J. Athas, J. S. Brooks, S. J. Klepper, S. Uji, and M. Tokumoto, Tunnel diode oscillator application to high sensitivity de Haas-van Alphen and superconducting critical field studies of anisotropic organic conductors, Rev. Sci. Instrum. **64**, 3248 (1993).

[26] T. Coffey, Z. Bayindir, J. F. DeCarolis, M. Bennett, G. Esper, and C. C. Agosta, Measuring radio frequency properties of materials in pulsed magnetic fields with a tunnel diode oscillator, Rev. Sci. Instrum. **71**, 4600 (2000).

[27] R. B. Clover and W. P. Wolf, Magnetic susceptibility measurements with a tunnel diode oscillator, Rev. Sci. Instrum. **41**, 617 (1970).

[28] T. Lancaster, P. A. Goddard, S. J. Blundell, F. R. Foronda, S. Ghannadzadeh, J. S. Möller, P. J. Baker, F. L. Pratt, C. Baines, L. Huang, J. Wosnitza, R. D. McDonald, K. A. Modic, J. Singleton, C. V. Topping, T. A. W. Beale, F. Xiao, J. A. Schlueter, A. M. Barton, R. D. Cabrera, *et al.*, Controlling magnetic order and quantum disorder in molecule-based magnets, Phys. Rev. Lett. **112**, 207201 (2014).

[29] J. Brambleby, P. A. Goddard, J. Singleton, M. Jaime, T. Lancaster, L. Huang, J. Wosnitza, C. V. Topping, K. E. Carreiro, H. E. Tran, Z. E. Manson, and J. L. Manson, Adiabatic physics of an exchange-coupled spin-dimer system: Magnetocaloric effect, zero-point fluctuations, and possible two-dimensional universal behavior, Phys. Rev. B **95**, 024404 (2017).

[30] H. Nojiri, H. Kageyama, Y. Ueda, and M. Motokawa, ESR study on the excited state energy spectrum of $SrCu_2(BO_3)_2$ – A central role of multiple-triplet bound states, J. Phys. Soc. Jpn. **72**, 3243 (2003).

[31] B. Leuenberger, A. Stebler, H. U. Güdel, A. Furrer, R. Feile, and J. K. Kjems, Spin dynamics of an isotropic singlet-ground-state antiferromagnet with alternating strong and weak interactions: An inelastic-neutron-scattering study of the dimer compound $Cs_3Cr_2Br_9$, Phys. Rev. B **30**, 6300 (1984).

[32] M. Kofu, J.-H. Kim, S. Ji, S.-H. Lee, H. Ueda, Y. Qiu, H.-J. Kang, M. A. Green, and Y. Ueda, Weakly coupled $S = 1/2$ quantum spin singlets in $Ba_3Cr_2O_8$, Phys. Rev. Lett. **102**, 037206 (2009).

[33] M. Kofu, H. Ueda, H. Nojiri, Y. Oshima, T. Zenmoto, K. C. Rule, S. Gerischer, B. Lake, C. D. Batista, Y. Ueda, and S. H. Lee, Magnetic-field induced phase transitions in a weakly coupled $S = 1/2$ quantum spin dimer system $Ba_3Cr_2O_8$, Phys. Rev. Lett. **102**, 177204 (2009).

[34] Z. Wang, D. Kamenskyi, O. Cépas, M. Schmidt, D. L. Quintero-Castro, A. T. M. N. Islam, B. Lake, A. A. Aczel, H. A. Dabkowska, A. B. Dabkowski, G. M. Luke, Y. Wan, A. Loidl, M. Ozerov, J. Wosnitza, S. A. Zvyagin, and J. Deisenhofer, High-field electron spin resonance spectroscopy of singlet-triplet transitions in the spin-dimer systems $Sr_3Cr_2O_8$ and $Ba_3Cr_2O_8$, Phys. Rev. B **89**, 174406 (2014).

[35] D. Kamenskyi, J. Wosnitza, J. Krzystek, A. A. Aczel, H. A. Dabkowska, A. B. Dabkowski, G. M. Luke, and S. A. Zvyagin, High-field ESR studies of the quantum spin dimer system $Ba_3Cr_2O_8$, J. Low Temp. Phys. **170**, 231 (2013).

[36] T. Nomura, Y. Skourski, D. L. Quintero-Castro, A. A. Zvyagin, A. V. Suslov, D. Gorbunov, S. Yasin, J. Wosnitza, K. Kindo, A. T. M. N. Islam, B. Lake, Y. Kohama, S. Zherlitsyn, and M. Jaime, Enhanced spin correlations in the Bose-Einstein condensate compound $Sr_3Cr_2O_8$, Phys. Rev. B **102**, 165144 (2020).

[37] H. Nojiri, H. Kageyama, K. Onizuka, Y. Ueda, and M. Motokawa, Direct observation of the multiple spin gap excitations in two-dimensional dimer system $SrCu_2(BO_3)_2$, J. Phys. Soc. Jpn. **68**, 2906 (1999).

[38] M. Tachiki and T. Yamada, Spin ordering in a spin-pair system, J. Phys. Soc. Jpn. **28**, 1413 (1970).

[39] Data featured in this paper are downloadable from the University of Warwick WRAP repository, Item 200652: https://wrap.warwick.ac.uk/200652/.